

Magnetotransport properties in epitaxial films of metallic delafossite PdCoO₂: Effects of thickness and width variations in Hall bar devices

Arnaud P. Nono Tchiomo^{†,1}, Anand Sharma^{‡,1}, Sethulakshmi Sajeed¹, Anna Scheid², Peter A. van Aken², Takayuki Harada³, and Prosper Ngabonziza^{1,4,*}

¹*Department of Physics and Astronomy, Louisiana State University, Baton Rouge, LA 70803, USA*

²*Max Planck Institute for Solid State Research, Heisenbergstr. 1, 70569 Stuttgart, Germany*

³*Research Center for Materials Nanoarchitectonics (MANA), National Institute for Materials Science, Tsukubashi, Ibaraki 305-0044, Japan*

⁴*Department of Physics, University of Johannesburg, P.O. Box 524 Auckland Park 2006, Johannesburg, South Africa*

(Dated: March 7, 2025)

We report on a combined structural and magnetotransport study of Hall bar devices of various lateral dimensions patterned side-by-side on epitaxial PdCoO₂ thin films. We study the effects of both the thickness of the PdCoO₂ film and the width of the channel on the electronic transport and the magnetoresistance properties of the Hall bar devices. All the films with thicknesses down to 4.88 nm are epitaxially oriented, phase pure, and exhibit a metallic behavior. At room temperature, the Hall bar device with the channel width $W = 2.5 \mu\text{m}$ exhibits a record resistivity value of $0.85 \mu\Omega\text{cm}$, while the value of $2.70 \mu\Omega\text{cm}$ is obtained in a wider device with channel width $W = 10 \mu\text{m}$. For the 4.88 nm thick sample, we find that while the density of the conduction electrons is comparable in both channels, the electrons move about twice as fast in the narrower channel. At low temperatures, for Hall bar devices of channel width $2.5 \mu\text{m}$ fabricated on epitaxial films of thicknesses 4.88 and 5.21 nm, the electron mobilities of ≈ 65 and $40 \text{ cm}^2\text{V}^{-1}\text{s}^{-1}$, respectively, are extracted. For thin-film Hall bar devices of width $10 \mu\text{m}$ fabricated on the same 4.88 and 5.21 nm thick samples, the mobility values of ≈ 32 and $18 \text{ cm}^2\text{V}^{-1}\text{s}^{-1}$ are obtained. The magnetoresistance characteristics of these PdCoO₂ films are observed to be temperature dependent and exhibit a dependency with the orientation of the applied magnetic field. When the applied field is oriented 90° away from the crystal c -axis, a persistent negative MR at all temperatures is observed; whereas when the field is parallel to the c -axis, the negative magnetoresistance is suppressed at temperatures above 150 K.

The delafossite oxides, with general molecular formula of ABO₂ (A=Pd or Pt), have captured significant attention due to their extraordinary electronic and structural properties. The key electronic characteristics include, for example, PtCoO₂ having the highest conductivity per carrier of all known materials and PdCoO₂ exhibiting the longest electron mean free path ($l_{e(T=4\text{ K})} = 21.4 \mu\text{m}$) for all known oxide materials [1–3]. The huge conductivity results from extremely broad conduction bands based on the $4d$ - $5s$ electrons of Pd, and the $5d$ - $6s$ electrons of Pt, whose character is nearly free electron like [3].

We focus on the PdCoO₂ delafossite material. The crystal structure of PdCoO₂ consists of two-dimensional (2D) Pd⁺ and [CoO₂]-layers alternated along the c -axis as shown in Fig. 1(a). The triangular coordinated Pd site layers are sandwiched between transition metal oxide layers in a stacking sequence [Fig. 1(b) - 1(c)]. The 2D Pd⁺ layers are electrically conductive, whereas the [CoO₂]-layers are electrically insulating. This quasi-2D layered crystal structure results in considerable anisotropy in electrical conduction. In single crystal samples, the room temperature ab -plane resistivity of $\rho_{ab} \approx 0.0026 \text{ m}\Omega \text{ cm}$ and c -axis resistivity of $\rho_c \approx 1.07 \text{ m}\Omega \text{ cm}$ were reported [3].

For fundamental research perspective, the combination of above interesting electronic characteristics together with its fascinating structural properties makes PdCoO₂ a promising material candidate for the investigation of fascinating and rich physics of the delafossite materials. Additionally, for technological applications, the high stability and mechanical rigidity of PdCoO₂ make it a promising electrode material for wide-bandgap semiconductor devices [4].

Although PdCoO₂ and related metallic delafossites were first synthesized in 1971 [5, 6], PdCoO₂ was largely ignored for decades. It is only in the mid 1990s that Tanaka and co-workers reported the growth of PdCoO₂ and PtCoO₂ crystals [7], as well as the first measurement of the temperature-dependent resistivity of PdCoO₂ [8]. This brought a renewed interest in PdCoO₂ material for studying its basic properties like the thermoelectric power [9–11], electronic structure [12–14] and high anisotropy in structure, conductivity and compression behavior [15–17]. However, the physics of PdCoO₂ has been primarily studied by using single crystal samples. Despite decades of research, these single crystals are still limited in size of $\approx 3 \text{ mm}$ in diameter [2, 18, 19]. Thus, to allow further studies of its physical properties, particularly as its thickness is decreased down to few unit cells, and the assessment of proof-of-principle spintronic devices, thin film samples with large area and smooth surfaces are desired.

* corresponding author: pngabonziza@lsu.edu

Recently, the thin films of metallic delafossites with thicknesses down to a few nanometers have been reported by several groups [4, 20–25]. These thin films were grown along the c -axis direction on substrates with pseudo-triangle lattices, such as Al_2O_3 (0001) [26–28] and $\beta\text{-Ga}_2\text{O}_3$ ($\bar{2}01$) [4, 29, 30]. The Al_2O_3 (0001) substrates have been mostly used for the thin-film growth of metallic delafossites [31]. Specifically, epitaxial PdCoO_2 films have been synthesized using sputtering [32, 33], pulsed-laser deposition (PLD) [21, 23, 34], molecular-beam epitaxy (MBE) [22, 24, 27, 28] and solid-phase reactions of precursors [25].

The magnetoresistance (MR) properties of PdCoO_2 have been characterized both in bulk single crystals [3] and in epitaxially-grown thin film prepared mostly on sapphire substrates [21–25, 27, 28, 32–34]. The MR data were only reported for a single (one) Hall bar device that was structured by focused ion beam on PdCoO_2 single crystals [35], and also for a single Hall bar device fabricated on epitaxial PdCoO_2 films [27, 34, 36]. However, patterning several Hall bar devices of various channel width side-by-side on the same PdCoO_2 sample offers an advantage over single crystal-based devices as it provides the opportunity to perform comparative study of magnetotransport properties from the same sample, measured in similar conditions [37]. Moreover, this practice is ideal for the exploration of lateral dimensional confinement effects in epitaxial films for tuning their electronic ground states.

In this paper, we report on a combined structural and magnetotransport study of Hall bar devices of various lateral sizes patterned side-by-side on the same PdCoO_2 thin film. In magnetotransport, we focus on exploring the effects of the film's thickness (t), the variation of the width (W) in Hall bar devices as well as the orientation of the magnetic field B on the MR characteristics. We use pulsed laser deposition (PLD) for the epitaxial growth of these thin films. The growth conditions are optimized to achieve phase-pure metallic delafossite PdCoO_2 thin films of different t down to a few nanometers. Subsequent structural analyses using x-ray diffraction (XRD) for unpatterned epitaxial films and high-resolution scanning transmission electron microscopy (STEM) for patterned Hall bar devices, confirm that these films and thin-film devices are epitaxially oriented and phase pure. The temperature dependence of the in-plane resistivity as a function of film thickness show metallic behavior down to ~ 4.88 nm.

For metallic delafossite PdCoO_2 of various t , we fabricated side-by-side on the same PdCoO_2 films several Hall bars of various W , and then explored their magnetotransport properties. In particular, for two Hall bar devices of channel width $W = 2.5$ and $10\ \mu\text{m}$, we found that the electron mobilities (μ_e), simultaneously extracted from Hall measurements at various temperatures, changed systematically as W and t were varied. At 2 K, we extracted μ_e values of ≈ 65 and $40\ \text{cm}^2\text{V}^{-1}\text{s}^{-1}$ from the Hall bar devices of $W = 2.5\ \mu\text{m}$ fabricated on epitaxial films of

$t = 4.88$ and 5.21 nm, respectively; whereas the μ_e values of ≈ 32 and $18\ \text{cm}^2\text{V}^{-1}\text{s}^{-1}$ were obtained from the devices with channel $W = 10\ \mu\text{m}$ fabricated on the same respective films. In addition, we find that the magnetotransport is strongly temperature dependent, and present a negative MR that can persist at all temperatures or switch to positive MR at certain temperatures depending on the orientation of the applied magnetic field with respect to the sample c -axis.

Epitaxial PdCoO_2 films were deposited on the (0001)-oriented Al_2O_3 ($c\text{-Al}_2\text{O}_3$) at a substrate temperature of $T_{\text{sub}} = 700\ ^\circ\text{C}$ under an oxygen pressure of $100 - 150$ mTorr in a PLD chamber using the 4th harmonic (266 nm) of Nd:YAG laser for ablation. PdCoO_2 and mixed-phase PdO_x targets were alternately ablated to obtain a stoichiometric composition. We prepared films of different thicknesses varying from 4.88 to 11.58 nm. The thickness of the PdCoO_2 films was determined using the thickness fringes around the PdCoO_2 (0006) peak in the XRD and the x-ray reflectivity data [20]. The electronic transport properties were measured by using a Quantum Design Physical Property Measurement System (PPMS), where a excitation current of $I = 1\ \mu\text{A}$ was applied to the Hall bars. The MR properties of the PdCoO_2 films were studied by changing the orientation of the magnetic field B such that $B \parallel c$, and B oriented 45° and 90° away from c . Details on the Hall bar device fabrication are provided in the supplemental material.

Figure 1(d) depicts XRD $2\theta - \omega$ scans of PdCoO_2 films of different thicknesses. This thickness-dependent analysis exhibits the crystal structure purity of the grown samples. The film reflections form only parallel (000 l) planes of the bulk crystal structure of PdCoO_2 , indicating an epitaxial and single phase growth along the c -axis. Additionally, the clear Laue oscillations observed around the film peaks suggest that the films have smooth surfaces. Note that as the thickness of the films increases (increasing unit cells), the films diffraction peaks become sharper. All these observations are consistent with previous reports on the epitaxial growth of PdCoO_2 thin films using PLD [21], MBE [22, 24, 27, 28], and sputtering [33].

We studied the structural perfection of the samples by performing symmetric rocking curve ω scans for the (0006) film peak as shown in Fig. 1(e). The full width at half maximum (FWHM) values extracted by fitting the rocking curves are plotted in Fig. 1(f). These small FWHM values hint at highly oriented PdCoO_2 films exhibiting minor out-of-plane misorientation [21, 24, 38]. It is noteworthy that other works on the heteroepitaxial growth of PdCoO_2 have reported azimuthal mosaicity (in-plane orientation distribution) by recording ϕ scans on asymmetric reflections. It was found that the PdCoO_2 films exhibit far greater mosaicity in the plane, and grow by forming twin domains which are rotated 180° from one another [see Fig. S1 of the supplemental material] and 30° from the Al_2O_3 substrate [21, 22, 24, 33]. Nevertheless, we consistently noted a small hump in the line shape of the main peak in the rocking curves of all the films

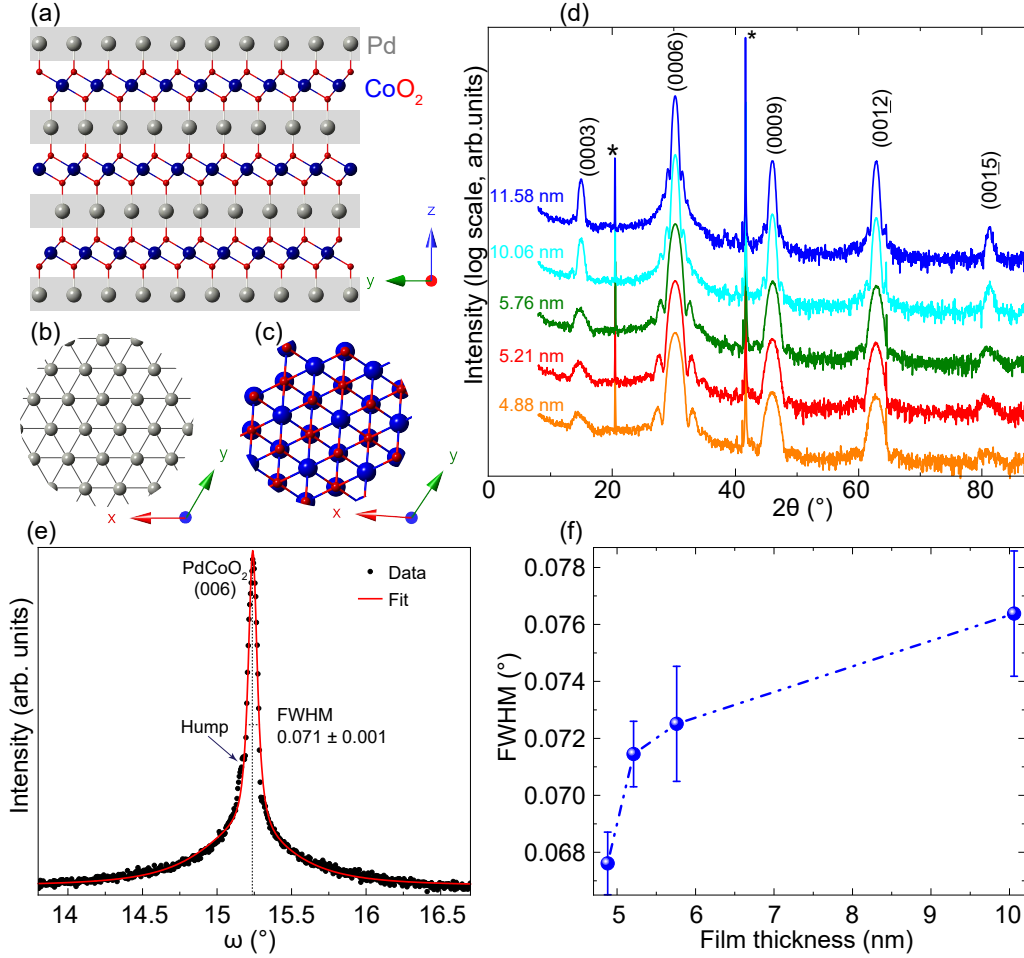


FIG. 1. **Structural characterizations of unpatterned PdCoO₂ films.** (a) A (100) atomic plane view of the crystal structure of delafossite PdCoO₂ presenting alternating stacks of highly conducting Pd and insulating CoO₂ layers. The layers are connected through O–Pd–O dumbbells. Both layers form triangular lattices as shown in the atomic (001) planes in (b) and (c), respectively for Pd and CoO₂. (d) Thickness-dependent $2\theta - \omega$ x-ray diffraction patterns of PdCoO₂ epitaxial films grown on (0001)–oriented Al₂O₃ substrates. The substrate peaks are indicated by asterisks (*) and the thickness of the films are indicated by the numbers adjacent to each XRD plot. (e) Rocking curve of a representative PdCoO₂ sample acquired around the main (006) film peak, and fitted to extract the full width at half maximum (FWHM). (f) Variation of the FWHM extracted from the (006) peak of the PdCoO₂ films shown in (d). Note the increase of the FWHM with increasing film thickness.

[see Fig. S2 of the supplemental material]. This could be an indication of an adjacent crystalline domain having a different orientation to the main crystalline block [39]. Our Scanning transmission electron microscopy (STEM) measurements provide evidence of twin boundaries in the PdCoO₂ film as discussed in the following.

Figure 2(c) presents the high-angle annular dark field (HAADF) STEM images of the PdCoO₂ film along the [210] orientation, obtained from a cross-section of a Hall bar device, as illustrated in Fig. 2(b). The magnified HAADF image reveals a sharp and smooth interface between the PdCoO₂ film and the Al₂O₃ substrate, consistent with the well-defined Laue oscillations observed in the XRD patterns [see, Fig. 1(d)] [24, 40]. Furthermore, the periodic layer stacking of the PdCoO₂ film confirms the presence of a pure delafossite phase. The crystallographic structures of both the film and substrate can be

overlaid on the simultaneously acquired HAADF and annular bright-field (ABF) images, which provide contrast for the lighter elements Al and O.

The STEM images indicate that the epitaxial relationship between the film and substrate is established through the initial [CoO₂][−] layer [Fig. 2(c)], which provides the low-energy interface for contact with the substrate, resulting in a stable heterointerface [24, 40, 41]. This is commonly achieved in the growth of delafossite PdCoO₂, PtCoO₂ and PdCrO₂ materials on the sapphire substrate using both PLD and MBE [21, 24, 27, 28]. Moreover, the HAADF STEM images along the [010] orientation [Fig. 2(d)] reveal domain boundaries, indicating the presence of stacking faults (S) and twin boundaries (T) in the film. The stacking faults correspond to the translational displacement of oxygen octahedra in successive delafossite layers; and, the twin boundaries de-

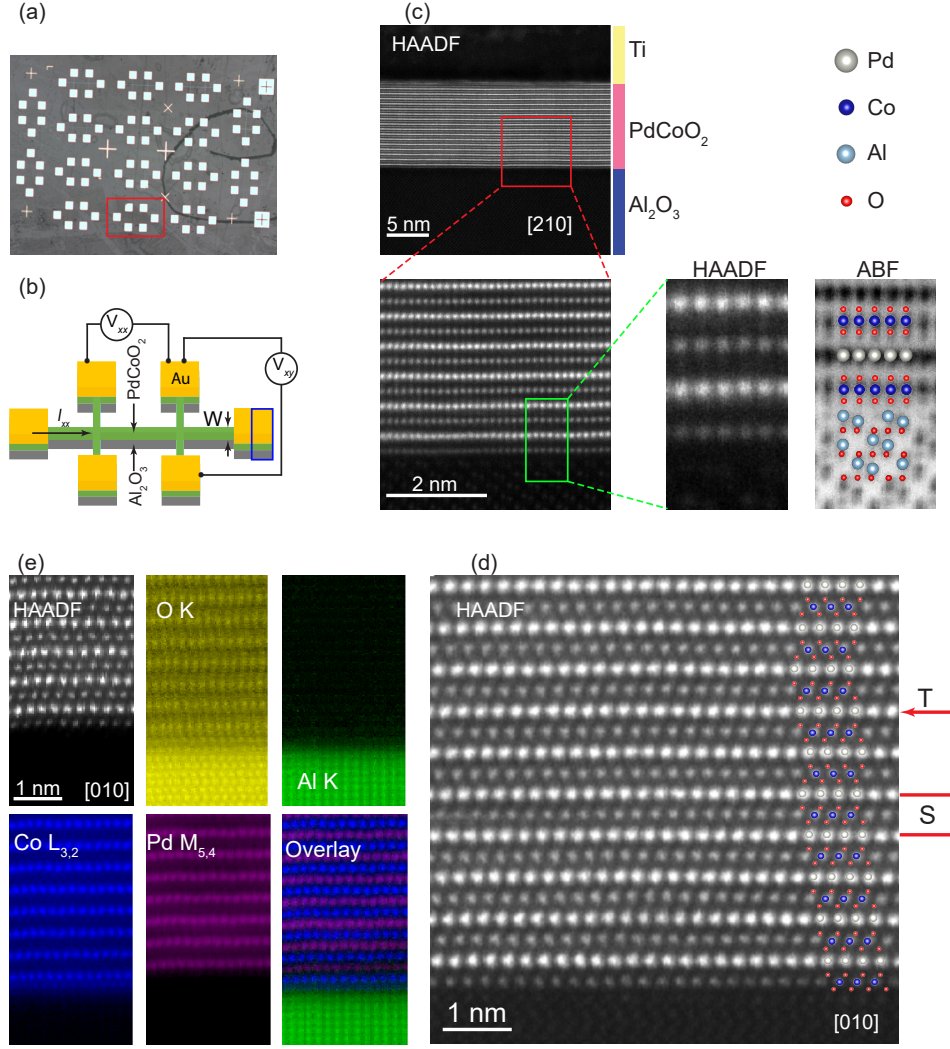


FIG. 2. **Device fabrication and Microstructural characterization of the PdCoO₂ sample grown on (0001)-oriented Al₂O₃ substrate using PLD.** (a) Optical micrograph image showing a top view of a whole PdCoO₂ sample on which several Hall bar devices of different channel widths (W) were fabricated side-by-side. The channel widths of these devices are $W = 10 \mu\text{m}$, $5 \mu\text{m}$, $2.5 \mu\text{m}$, $1 \mu\text{m}$ and 500 nm . (b) Schematic illustration of a typical Hall bar device (red rectangle in (a)) indicating the transport measurement configuration. (c) Cross-sectional HAADF-STEM image obtained from a Hall bar device as indicated by the blue rectangle in (b). The enlarged insets show the atomic-scale structure of the delafossite-substrate interface along the [210] orientation of the film with an structural overlay of the atomic models on simultaneously acquired HAADF and ABF images. The HAADF STEM images provide strong contrast for the heavier elements Pd and Co, while the O and Al atomic columns are only visible in the ABF images capturing electrons scattered toward lower angles. (d) HAADF STEM image along the [010] orientation of the film reveals domains with opposing orientations of the CoO₆ octahedra in subsequent [CoO₂]⁻ layers indicating the presence of twins T (red arrow), and stacking faults S. (e) EELS elemental mapping across the PdCoO₂/Al₂O₃ interface obtained by extracting the respective edge signals from a 2D spectrum image across the [010] zone axis, indicating a sharp film-substrate interface.

pict the mirrored orientation of the oxygen octahedra in adjacent layers. These features are commonly observed in delafossite thin films grown on *c*-axis-oriented substrates [21, 22, 24, 42].

EELS elemental mapping across the PdCoO₂/Al₂O₃ interface, shown in Fig. 2(e), reveals the atomic elemental distribution along the [010] orientation of the film. The extraction of element-specific energy loss edge signals enables the mapping of the delafossite structure composi-

tion. The absence of intermixed layers at the interface suggests that the film exhibits good stoichiometry [43], and confirms its epitaxial growth. The EELS elemental maps further verify that the film nucleates with a [CoO₂]⁻ layer.

The PdCoO₂ samples also exhibit good electrical characteristics over the varying thicknesses as portrayed in the temperature dependence of the resistivity at zero magnetic field presented in Fig. 3, for the Hall bar de-

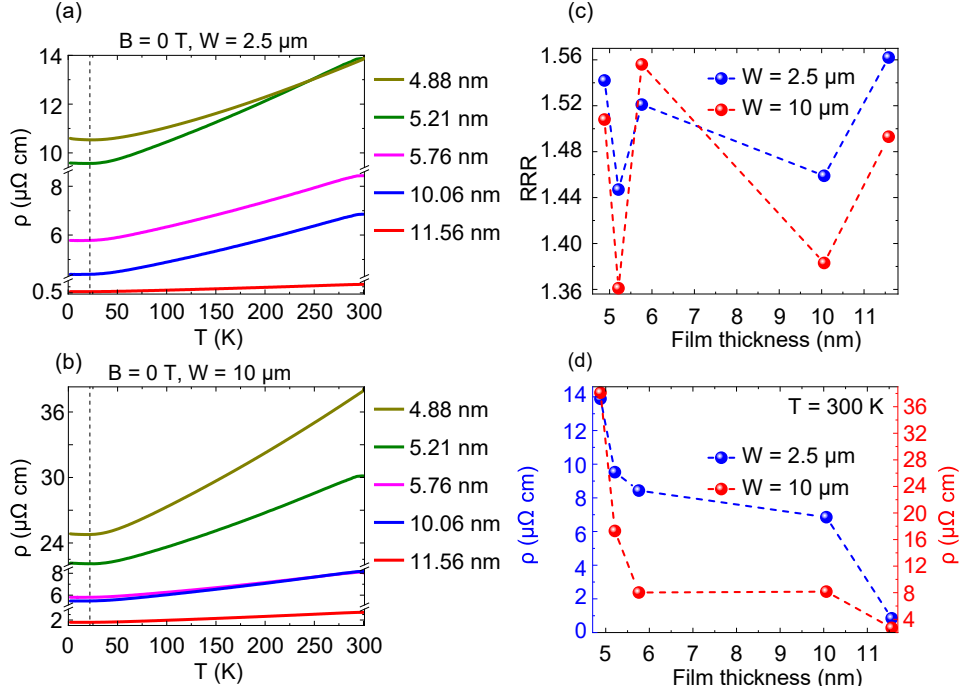


FIG. 3. **Thickness-dependent electronic transport characteristics of PdCoO₂ epitaxial films.** (a) and (b) Temperature dependent resistivity at zero magnetic field for patterned PdCoO₂ Hall bar thin-film devices for a range of thicknesses. The channel widths are (a) $w = 2.5 \mu\text{m}$ and (b) $w = 10 \mu\text{m}$. The vertical dashed lines indicate $T_{\min} = 20$ K. The patterned Hall bar devices in (a) and (b) were fabricated side-by-side on the same PdCoO₂ films in which electronic transport properties were studied. (c) Plot of the variation of the residual resistivity ratio (RRR) as $\rho_{300 \text{ K}}/\rho_{2 \text{ K}}$ VS films thickness for both Hall bar widths. (d) Variation of the room temperature (RT) resistivity values as a function of the film's thickness for both Hall bar geometries. The RRR and the RT resistivity values plotted in (c) and (d), respectively, are extracted from (a) and (b). Note that the overall trend with respect to both Hall bar device widths is that the confinement of charge carriers in a narrower channel results in improved electronic properties, as the scattering pathway is reduced.

vices with channel widths 2.5 and 10 μm . The resistivity is seen to decrease with increasing film's thickness. For each sample, the resistivity displays a positive temperature coefficient, consistently for the two Hall bar devices [Fig. 3(a) and 3(b)]. This is indicative of a metallic behavior in all the films over almost the entire temperature range [44, 45]. However, in the low temperature regions, $T \leq 20$ K, and for all the samples in both device geometries, the residual resistivity is substantially the total resistivity, as the plots are all nearly straight horizontal lines. This saturation is the result of the low temperature effect in nearly pure metallic compounds as outlined by the Matthiessen's rule: To the first approximation, the residual resistivity is governed by scattering of impurities, whose contributions constitute an additive effect to the resistivity and are independent of temperature [46–48]. Nonetheless, deviations from the Matthiessen's rule are observed at higher temperatures ($T > 20$ K), as the temperature-dependent component of the resistivity increases in magnitude with decreasing film's thickness [see Fig. S7 of the supplemental material]. Similar thickness-dependent electrical resistivity behavior was reported for MBE grown PdCoO₂ thin films [49]. In addition, the effective mass was found to considerably increase with decreasing film's thickness. It was suggested that, as thin-

ner films exhibit larger surface scattering fraction and higher in-plane defects concentration, disorder-enhanced electron-phonon scattering could be one of the possible mechanisms behind the observed deviations [49]. Note that for bulk pure and nearly pure metals such as Pd, Au, Cu, and Ag, temperature-dependent electrical resistivity analogous to that discussed here has been reported [46].

It is remarkable that the temperature minimum ($T_{\min} = 20$ K) at which the resistivity starts to plateau (yielding the minimum resistivity) is constant regardless of the thickness of the films and the device width [Fig. 3(a) and 3(b)]. This suggests that the low temperatures transport properties of these films with thicknesses up to about 12 nm are mostly limited by inherent crystallographic defects, which are potentially of equal concentration [46, 47]. In particular, a shallow increase in the resistivity below T_{\min} associated with disorder-induced localization effects in the PdCoO₂ films was reported in a recent study [22]. It was observed that annealing of the PdCoO₂ films leads to a drop in T_{\min} and to improved electrical characteristics owing to the reduction of the density of defects in the films [22].

Additionally, since the presence of impurities or defects in metals make these systems more resistive at low temperature [46], the residual resistivity ratio (RRR) for

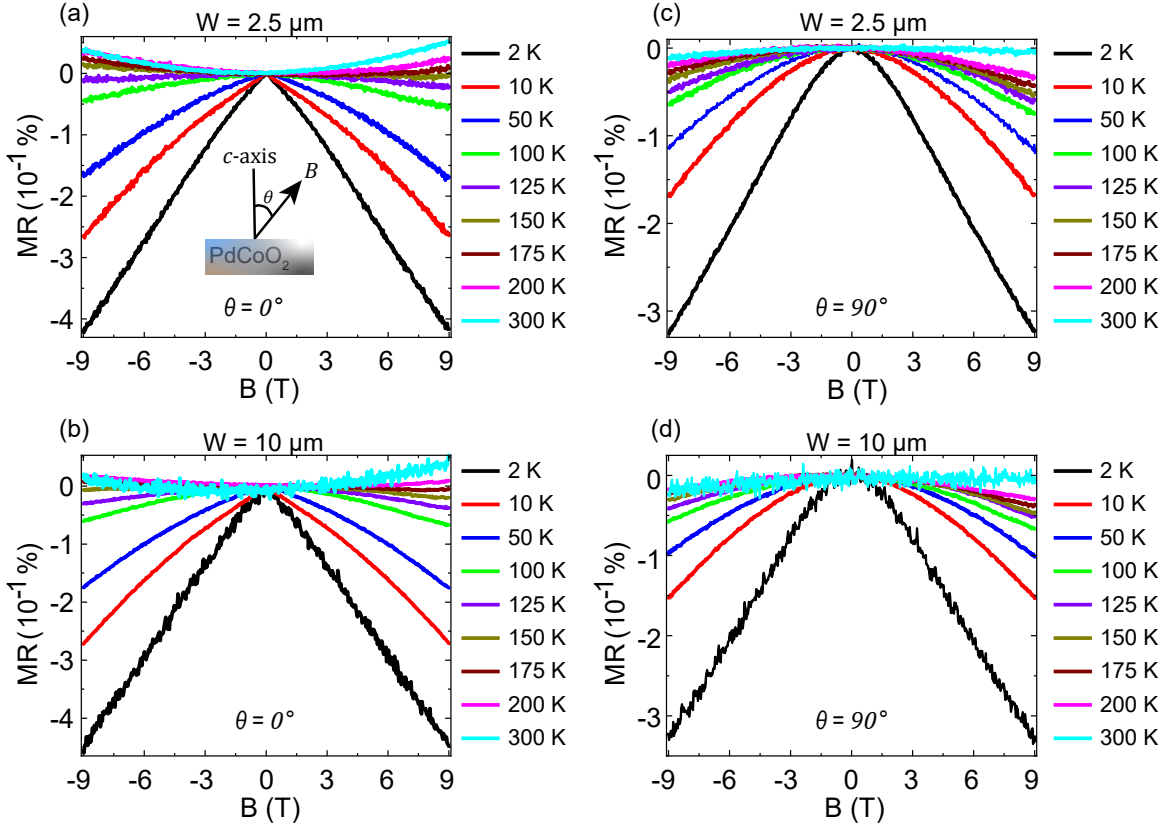


FIG. 4. **Temperature-dependent magnetoresistance (MR) properties of epitaxial PdCoO₂ films measured at different B orientations.** The data are from two Hall bar devices of channel widths $W = 2.5 \mu\text{m}$ and $W = 10 \mu\text{m}$ fabricated on the PdCoO₂ sample with thickness $t = 4.88 \text{ nm}$. (a) and (b) MR simultaneously acquired when $B \parallel c$, ie, $\theta = 0^\circ$. (c) and (d) MR simultaneously acquired when $B \perp c$, ie, $\theta = 90^\circ$. The insert in (a) shows the orientation of B with respect to the c -axis. Note that when $\theta = 0^\circ$, the MR present a cross-over from negative to positive at temperatures above 150 K; but when $\theta = 90^\circ$, the negative MR persist at all temperatures. Note that through out the magnetotransport measurements, B is always perpendicular to I .

a temperature close to absolute zero ($\rho_{300 \text{ K}}/\rho_{2 \text{ K}}$) represents a very sensitive gauge to structural disorder in the PdCoO₂ films. The maximum RRR of 1.56 for our thickest PdCoO₂ films (11.56 nm) is two orders of magnitude smaller than that of pure bulk single crystals [19], but comparable to those recently reported for PLD and MBE grown PdCoO₂ films at similar thicknesses [21–24] [Fig. 3(c)]. Moreover, the RRR seems to be independent of the thickness of the films. This is contrary to the almost linear trend reported for MBE grown PdCoO₂ films where it was indicated that surface scattering mechanisms including scattering at the twin boundaries and film-substrate interface have a larger contribution to the low temperature electrical resistance [22, 24].

The variation of the room temperature (RT) resistivity values as a function of the film's thickness for both device widths is plotted in Fig. 3(d). A record value of $0.85 \mu\Omega\text{cm}$ is achieved in the device with the narrower width, while a value of $2.70 \mu\Omega\text{cm}$ is obtained in the device with the wider width. The former value is one order of magnitude smaller than any value reported so far for the epitaxial growth of PdCoO₂ thin films [21, 22, 24];

and the latter value is somewhat equal to the RT resistivity value of bulk pure single crystals [1, 3, 35]. It is however important to highlight that the comparatively low electrical properties of our PdCoO₂ thin films, especially the low RRR, stem from the presence of additional structural defects in the film such as dislocations, which originate from the large lattice mismatch between the PdCoO₂ film and the Al₂O₃ substrate [36].

The magnetoresistance (MR) responses of our 4.88 nm thick PdCoO₂ film measured at temperatures ranging from 2 K to 300 K with the magnetic field $B \parallel c$ ($\theta = 0^\circ$) and oriented 90° away from c ($\theta = 90^\circ$) are shown in Fig. 4 for both Hall bar devices. It can be seen that the MR is strongly temperature dependent. When $\theta = 0^\circ$, ie, transverse MR [Fig. 4(a) and (b)], the magnetotransport presents two distinct regimes. At temperatures below 150 K, both devices exhibit negative MR which increases with decreasing temperature down to 2 K. This negative MR which is more pronounced at low temperatures ($\leq 50 \text{ K}$) could be thought to originate from the weak localization of the electrons in the PdCoO₂ sample. Weak localization is known to be an anomalous quan-

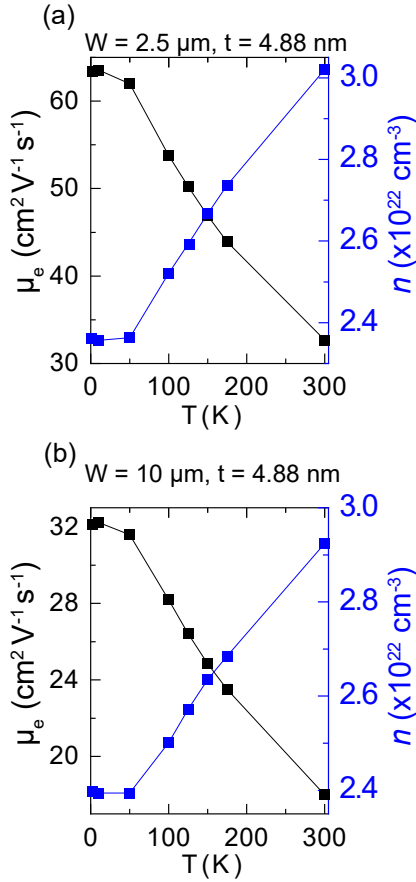


FIG. 5. **Electron mobility (μ_e) and carrier density (n) as a function of temperature.** Electronic transport characteristics of the Hall bar devices with channel widths (a) $W = 2.5 \mu\text{m}$ and (b) $W = 10 \mu\text{m}$ fabricated on PdCoO₂ epitaxial films of thickness $t = 4.88$ nm. These data were simultaneously extracted from Hall effect measurements with $B \perp I$, *i.e.*, $\theta = 0^\circ$. The narrower channel $W = 2.5 \mu\text{m}$ yields μ_e values that are about twice those of the wider channel $W = 10 \mu\text{m}$, while the n values are comparable.

tum phenomenon observed in the transport properties of disordered 2D systems [50]. It has been reported to essentially originates from the quantum interference of the conduction electrons on the defects of the systems [50]. However, when comparing the lineshapes of our negative MR data [see, Fig. 4] with those of negative MR associated with the weak localization effect at comparable magnetic field strengths [see Refs. [27, 50]], it is evident that a different mechanism governs the negative MR in our PdCoO₂ films.

For longitudinal MR measurement ($B \parallel I$) on a ultra-clean PdCoO₂ single crystal sample and for a magnetic field strength up to 9 T, Kikugawa *et al.* [51] observed a negative MR at 1.4 K, similar to the low temperatures MR shown in Fig. 4. They argued that this negative MR could not be caused by scattering at magnetic impurities and explained in terms of weak localization effects, given the magnitude of the measured MR, the high pu-

urity as well as the non-magnetic property of the sample. This claim was supported by showing that for $B \perp I$ (transverse MR), large and positive (at all temperatures down to 1.4 K) MR could be achieved. The authors rather attributed the observed negative MR to the emergence of the axial anomaly between the Fermi points of a field induced one dimensional electronic dispersion in PdCoO₂ [51]. Given the measurement geometry of the data in Fig. 4 where the current was always perpendicular to the sample c -axis, we would believe that a different underlying quantum mechanism could be driving the negative MR in our data. Furthermore, we exclude the possibility of weak localization effects since our PdCoO₂ samples present no evidence of surface magnetism [see Fig. S7 of the supplemental material] such as the surface ferromagnetism previously reported in an ultrathin (3.8 nm) PdCoO₂ film [36]. The absence of magnetism in our PdCoO₂ samples is possibly due to the mixed termination of the surface, as indicated by the relatively rough surface [see Fig. S1 of the supplemental material].

It is interesting that for the same longitudinal MR measurement by Kikugawa *et al.*, the negative MR is progressively suppressed by increasing the temperature, but does not completely vanishes at the highest temperature of 300 K [51]. This is consistent with the MR response shown in Fig. 4(c) and (d) for MR measurements with $B \perp c$, *i.e.*, when $\theta = 90^\circ$. These observations suggest that the driving mechanism of the negative MR would not be suppressed when $B \perp c$, regardless of the increased thermal energy which triggers resistive mechanisms such as electron-phonon interaction. This is in contrast to the MR response presented in Fig. 4(a) and (b) ($\theta = 0^\circ$, $B \parallel c$). There, as the temperature increases, the lineshape of the MR progresses towards a more quadratic dependence from low temperatures where the MR is negative to temperatures beyond 150 K where the MR becomes positive. Positive MR is believed to be dominated by classical orbital magnetoresistive effects associated with scattering from impurities and phonons. It is remarkable that these magnetoresistive effects kick in at earlier temperatures in the thickest measured sample, $t = 11.56$ nm. Positive MR are observed at temperatures > 125 K [see Fig. S3 of the supplemental material]. It is important to highlight that the temperature dependent magnetotransport properties of the 4.88 nm and 5.21 nm samples are comparable, regardless of the orientation of B [see Fig. 4, and Fig. S4 and S5 of the supplemental material]. Note that a similar temperature-dependent MR cross-over was recently reported in a PLD grown PdCoO₂ thin film [36].

Figure 5 depicts the evolution with temperature of the electron mobility, μ_e , and the carrier density, n , of the two Hall bar with indicated channel widths for the same PdCoO₂ sample studied in Fig. 4. Two distinct regimes can be identified for n : A regime at temperatures between 300 K and 50 K where the carrier densities drop by $\approx 20\%$ in cooling; and a regime at temperatures below 50 K where the carrier densities are independent of

the temperature. These behaviors are consistent with previous reports on the temperature dependence of n in epitaxial PdCoO₂ films [36, 49, 52]. It is however noteworthy that the strong dependence of n to high temperatures could be inferred to the level of disorder/defect in the film at high temperatures, which is also associated with sizable changes in the effective mass as discussed above. Hence, it could be that the Hall coefficient at high temperature for this class of material may not reflect the actual carrier density [35, 49].

The extracted μ_e range between ≈ 18 and ≈ 65 cm²V⁻¹s⁻¹ in both Hall bar devices from RT to 2 K. This range of electron mobility values is consistent with the small amplitudes of the MR at the field strength of 9 T and for the respective temperatures [36, 53]. In the sample with $t = 5.21$ nm and for both Hall bar channels [see Fig. S8 of the supplemental material], the carrier densities also drop by $\approx 20\%$ in a single regime from 300 K to 2 K. The electron mobilities vary from ≈ 10 to ≈ 40 cm²V⁻¹s⁻¹ while cooling from RT down to 2 K, which are consistent with a recent report [36].

In this study, we have reported the structural, microstructural and magnetotransport properties of Hall bar devices of various widths, fabricated on epitaxial PdCoO₂ films of different thicknesses. We have analyzed two Hall bar geometries of width $W = 2.5$ and 10 μ m, all structured into the same delafossite PdCoO₂ thin films of various thicknesses. The PLD prepared PdCoO₂ samples exhibit good structural quality with sharp interfaces that present no signs of atomic interdiffusion. In addition, both Hall bar devices exhibit transport characteristics, ρ , n , and μ_e , that are comparable to those re-

ported in the literature. For the device geometries discussed in this work, we found that the narrower Hall bar, $W = 2.5$ μ m, displays slightly better electronic transport performances as compared to the wider 10 μ m Hall bar. Furthermore, we have demonstrated that the MR properties of the PdCoO₂ samples are strongly temperature dependent, but show no variation with either the thickness of the film or the geometry of the Hall bar device. Moreover, we have noted a persistent negative MR when $B \perp c$ at all temperatures from 2 to 300 K. For transverse MR, $B \parallel c$, the negative MR is suppressed at temperatures above 150 K, and the MR progresses toward a more parabolic dependence, characteristic of classical orbital magnetoresistance. The lineshapes of our MR data suggest that some underlying quantum phenomenon, other than weak localization effects, would be at the origin of the emergence of this negative MR in our PdCoO₂ samples, especially because these samples are non magnetic. An attempt to unravel this would be to carry out a systematic study which combines theory and experiment. The results of this study provide additional basis for the understanding of the MR in PdCoO₂ which has proved to be highly dependent on the orientation of the magnetic field, a property that could be relevant to certain applications.

ACKNOWLEDGMENTS

P. Ngabonziza. acknowledges startup funding from the College of Science and the Department of Physics & Astronomy at Louisiana State University. The authors acknowledge Dr Julia Deuschle for the FIB sample preparation for the STEM investigations.

-
- [1] C. W. Hicks, A. S. Gibbs, A. P. Mackenzie, H. Takatsu, Y. Maeno, and E. A. Yelland, *Phys. Rev. Lett.* **109**, 116401 (2012).
 - [2] P. Kushwaha, V. Sunko, P. J. W. Moll, L. Bawden, J. M. Riley, N. Nandi, H. Rosner, M. P. Schmidt, F. Arnold, E. Hassinger, T. K. Kim, M. Hoesch, A. P. Mackenzie, and P. D. C. King, *Sci. Adv.* **1**, e1500692 (2015).
 - [3] A. P. Mackenzie, *Rep. Prog. Phys.* **80**, 032501 (2017).
 - [4] T. Harada, S. Ito, and A. Tsukazaki, *Sci. Adv.* **5**, eaax5733 (2019).
 - [5] R. D. Shannon, D. B. Rogers, and C. T. Prewitt, *Inorg. Chem.* **10**, 713 (1971).
 - [6] D. R. C.T. Prewitt, R.D. Shannon, *Inorg. Chem.* **10**, 719 (1971).
 - [7] M. Tanaka, M. Hasegawa, and H. Takei, *J. Cryst. Growth* **173**, 440 (1997).
 - [8] M. Tanaka, M. Hasegawa, and H. Takei, *J. Phys. Soc. Jpn.* **65**, 3973 (1996).
 - [9] M. Hasegawa, I. Inagawa, M. Tanaka, I. Shirotnani, and H. Takei, *Solid State Commun.* **121**, 203 (2002).
 - [10] K. P. Ong, D. J. Singh, and P. Wu, *Phys. Rev. Lett.* **104**, 176601 (2010).
 - [11] M. E. Gruner, U. Eckern, and R. Pentcheva, *Phys. Rev. B* **92**, 235140 (2015).
 - [12] K. Kim, H. C. Choi, and B. I. Min, *Phys. Rev. B* **80**, 035116 (2009).
 - [13] V. Eyert, R. Frésard, and A. Maignan, *Chem. Mater.* **20**, 2370 (2008).
 - [14] K. P. Ong, J. Zhang, J. S. Tse, and P. Wu, *Phys. Rev. B* **81**, 115120 (2010).
 - [15] R. Daou, R. Frésard, S. Hébert, and A. Maignan, *Phys. Rev. B* **91**, 041113 (2015).
 - [16] H.-J. Noh, J. Jeong, J. Jeong, E.-J. Cho, S. B. Kim, K. Kim, B. I. Min, and H.-D. Kim, *Phys. Rev. Lett.* **102**, 256404 (2009).
 - [17] M. Hasegawa, M. Tanaka, T. Yagi, H. Takei, and A. Inoue, *Solid State Commun.* **128**, 303 (2003).
 - [18] R. D. Shannon, C. T. Prewitt, and D. B. Rogers, *Inorg. Chem.* **10**, 719 (1971).
 - [19] H. Takatsu, S. Yonezawa, S. Mouri, S. Nakatsuji, K. Tanaka, and Y. Maeno, *J. Phys. Soc. Jpn.* **76**, 104701 (2007).
 - [20] T. Harada, K. Sugawara, K. Fujiwara, M. Kitamura, S. Ito, T. Nojima, K. Horiba, H. Kumigashira, T. Takahashi, T. Sato, and A. Tsukazaki, *Phys. Rev. Res.* **2**, 013282 (2020).
 - [21] T. Harada, K. Fujiwara, and A. Tsukazaki, *APL Mater.* **6**, 046107 (2018).

- [22] M. Brahlek, G. Rimal, J. M. Ok, D. Mukherjee, A. R. Mazza, Q. Lu, H. N. Lee, T. Z. Ward, R. R. Unocic, G. Eres, and S. Oh, *Phys. Rev. Mater.* **3**, 093401 (2019).
- [23] P. Yordanov, W. Sigle, P. Kaya, M. E. Gruner, R. Pentcheva, B. Keimer, and H.-U. Haberman, *Phys. Rev. Mater.* **3**, 085403 (2019).
- [24] J. Sun, M. R. Barone, C. S. Chang, M. E. Holtz, H. Paik, J. Schubert, D. A. Muller, and D. G. Schlom, *APL Mater.* **7**, 121112 (2019).
- [25] R. Wei, P. Gong, M. Zhao, H. Tong, X. Tang, L. Hu, J. Yang, W. Song, X. Zhu, and Y. Sun, *Adv. Funct. Mater.* **30**, 2002375 (2020).
- [26] T. Kawamoto, A. Krishnadas, C.-H. Hsu, M. Pardo-Almanza, Y. Fujisawa, G. Chang, T. Harada, and Y. Okada, *Phys. Rev. Mater.* **7**, 024001 (2023).
- [27] Q. Song, J. Sun, C. T. Parzyck, L. Miao, Q. Xu, F. V. E. Hensling, M. R. Barone, C. Hu, J. Kim, B. D. Faeth, H. Paik, P. D. C. King, K. M. Shen, and D. G. Schlom, *APL Mater.* **10**, 091113 (2022).
- [28] Q. Song, Z. He, B. D. Faeth, C. T. Parzyck, A. Scheid, C. J. Mowers, Y. Feng, Q. Xu, S. Hasko, J. Park, M. R. Barone, Y. E. Suyolcu, P. A. van Aken, B. Pamuk, C. J. Fennie, P. D. C. King, K. M. Shen, and D. G. Schlom, *APL Mater.* **12**, 081117 (2024).
- [29] T. Harada and A. Tsukazaki, *APL Materials* **8**, 041109 (2020).
- [30] T. Harada and A. Tsukazaki, *Applied Physics Letters* **116**, 232104 (2020).
- [31] T. Harada, *Mater. Today Adv.* **11**, 100146 (2021), and references therein.
- [32] P. F. Carcia, R. D. Shannon, P. E. Bierstedt, and R. B. Flippen, *JES* **127**, 1974 (1980).
- [33] T. Harada, T. Nagai, M. Oishi, and Y. Masahiro, *J. Appl. Phys.* **133**, 085302 (2023).
- [34] T. Harada, P. Bredol, H. Inoue, S. Ito, J. Mannhart, and A. Tsukazaki, *Phys. Rev. B* **103**, 045123 (2021).
- [35] N. Nandi, T. Scaffidi, P. Kushwaha, S. Khim, M. E. Barber, V. Sunko, F. Mazzola, P. D. C. King, H. Rosner, P. J. W. Moll, M. König, J. E. Moore, S. Hartnoll, and A. P. Mackenzie, *npj Quantum Mater.* **3**, 66 (2018).
- [36] J. H. Lee, T. Harada, F. Trier, L. Marcano, F. Godel, S. Valencia, A. Tsukazaki, and M. Bibes, *Nano Lett.* **21**, 8687 (2021).
- [37] P. Ngabonziza, A. Sharma, A. Scheid, S. Sajeev, P. A. van Aken, and J. Mannhart, *Phys. Rev. Mater.* **8**, 044401 (2024).
- [38] S. Acharya, A. Chatterjee, V. Bhatia, A. I. K. Pillai, M. Garbrecht, and B. Saha, *Mater. Res. Bull.* **143**, 111443 (2021).
- [39] S. Dolabella, A. Borzi, A. Dommann, and A. Neels, *Small Methods* **6**, 2100932 (2022).
- [40] A. Scheid, T. Heil, Y. E. Suyolcu, N. Enderlein, A. P. N. Tchiomo, P. Ngabonziza, P. Hansmann, D. G. Schlom, P. A. van Aken, *et al.*, arXiv preprint arXiv:2502.13727 (2025).
- [41] J. M. Ok, M. Brahlek, W. S. Choi, K. M. Roccapiore, M. F. Chisholm, S. Kim, C. Sohn, E. Skoropata, S. Yoon, J. S. Kim, *et al.*, *APL Mater.* **8**, 051104 (2020).
- [42] J. Roudebush, N. H. Andersen, R. Ramlau, V. O. Garlea, R. Toft-Petersen, P. Norby, R. Schneider, J. Hay, and R. Cava, *Inorg. Chem.* **52**, 6083 (2013).
- [43] A. P. Nono Tchiomo, E. Carleschi, A. R. Prinsloo, W. Sigle, P. A. Van Aken, J. Mannhart, P. Ngabonziza, and B. P. Doyle, *AIP Adv.* **12**, 105019 (2022).
- [44] A. P. Nono Tchiomo, W. Braun, B. P. Doyle, W. Sigle, P. Van Aken, J. Mannhart, and P. Ngabonziza, *APL Mater.* **7**, 041119 (2019).
- [45] A. P. Nono Tchiomo, *Electronic band structure and transport studies of oxide materials* (University of Johannesburg (South Africa), 2020).
- [46] R. A. Matula, *J. Phys. Chem. Ref. Data* **8**, 1147 (1979).
- [47] M. Cimberle, G. Bobel, and C. Rizzuto, *Adv. Phys.* **23**, 639 (1974).
- [48] J. Bass, *Adv. Phys.* **21**, 431 (1972).
- [49] D. Barbalas, A. Legros, G. Rimal, S. Oh, and N. Armitage, *Phys. Rev. B* **106**, 115113 (2022).
- [50] G. Bergmann, *Phys. Rep.* **107**, 1 (1984).
- [51] N. Kikugawa, P. Goswami, A. Kiswandhi, E. Choi, D. Graf, R. Baumbach, J. Brooks, K. Sugii, Y. Iida, M. Nishio, *et al.*, *Nature Commun.* **7**, 10903 (2016).
- [52] T. Harada, P. Bredol, H. Inoue, S. Ito, J. Mannhart, and A. Tsukazaki, *Phys. Rev. B* **103**, 045123 (2021).
- [53] C. Shekhar, A. K. Nayak, Y. Sun, M. Schmidt, M. Nicklas, I. Leermakers, U. Zeitler, Y. Skourski, J. Wosnitza, Z. Liu, *et al.*, *Nature Phys.* **11**, 645 (2015).

Supplementary material:

Magnetotransport properties in epitaxial films of metallic delafossite PdCoO_2 : Effects of thickness and width variations in Hall bar devices

Arnaud P. Nono Tchiomo¹⁾, Anand Sharma¹⁾, Sethulakshmi Sajeev¹⁾, Anna Scheid²⁾, Peter A. van Aken²⁾, Takayuki Harada³⁾, Prosper Ngabonziza^{1,4)}

¹⁾*Department of Physics and Astronomy, Louisiana State University, Baton Rouge, LA 70803, USA*

²⁾*Max Planck Institute for Solid State Research, Heisenbergstr. 1, 70569 Stuttgart, Germany*

³⁾*Research Center for Materials Nanoarchitectonics (MANA), National Institute for Materials Science, Tsukubashi, Ibaraki 305-0044, Japan*

⁴⁾*Department of Physics, University of Johannesburg, P.O. Box 524 Auckland Park 2006, Johannesburg, South Africa*

I. DESIGN OF THE HALL BAR DEVICES

PdCoO_2 thin films of various thicknesses were epitaxially grown on Al_2O_3 substrates using optimized deposition conditions to ensure high crystallinity and uniformity across each sample. These films were then patterned into Hall bar devices with channel widths ranging from 500 nm to 10 μm , allowing us to investigate the impact of device geometry on electronic and magnetotransport properties. Standard optical lithography (MW3) was employed to achieve precise patterning, resulting in well-defined Hall bar structures that enabled reliable transport measurements. To establish stable electrical contacts, each device was designed with Ti and Au layers of 5 and 45 nm, respectively, deposited via electron-beam evaporation. This provided robust charge injection capabilities suitable for measurements across a broad temperature range. Top-view scanning electron microscopy (SEM) verified the patterning accuracy and the structural integrity of the devices, while a side-view schematic of the devices illustrated the arrangement of the PdCoO_2 films on the Al_2O_3 substrate (see main text). Aluminum wire bonding was used to establish durable connections at the device corners, which remained reliable throughout extensive temperature cycling and repeated measurements.

II. STEM DATA ACQUISITION

Electron-transparent TEM specimens of the sample were prepared on a FEI Scios focused ion beam (FIB) using the standard lift-out method. Samples with a size of $20 \times 5 \mu\text{m}^2$ were thinned to 30 nm with 5 kV Ga ions, followed by a final polish at 2 kV to reduce the effects of surface damage.

STEM investigations were performed using a JEOL JEM-ARM200F equipped with a cold field-emission gun and a probe Cs corrector (DCOR, CEOS GmbH). The measurements were performed at ambient temperature with an acceleration voltage of 200 kV. In order to improve the signal-to-noise ratio, reduce scanning artifacts, and address sample drift effects, the STEM images were generated from multi-frame acquisitions using high scanning speeds and applying post-acquisition cross-correlation. In addition, strategic rotation of the scan window with respect to the atomic lattice was implemented to avoid superposition of lattice peaks in the Fourier transform with features associated with scan artifacts.

The EELS data were acquired using a Gatan GIF Quantum ERS imaging filter with a 5 mm entrance aperture and a 1.5 cm camera length, resulting in a collection semi-angle of 111 mrad. Principal component analysis (PCA) was used to improve the signal-to-noise ratio, and 15 principal components were used for accurate elemental mapping [1].

III. AFM AND XRD ROCKING CURVES

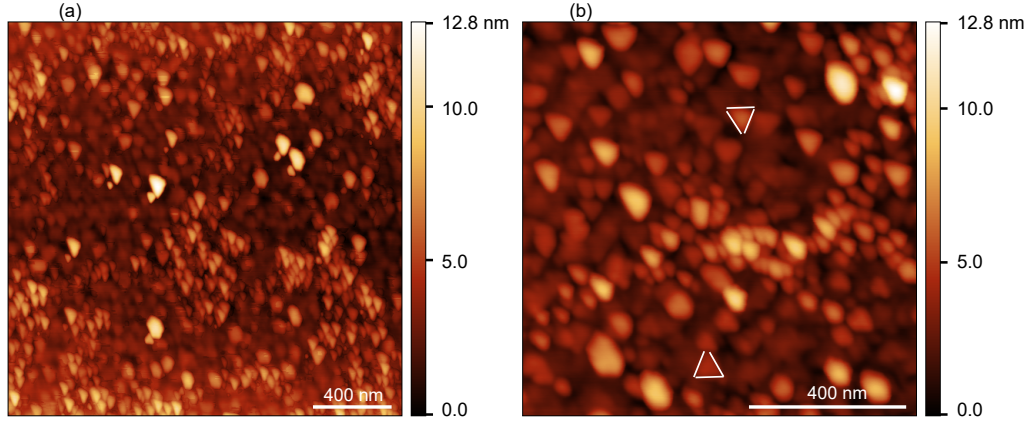


Figure S1: Atomic force microscopy (AFM) images of a representative PdCoO_2 sample. (a) Triangular structures are visible at the surface. (b) Zoomed AFM image depicting two triangular features rotated 180° from one another. This is an evidence of the existence of twin domains in the PdCoO_2 film.

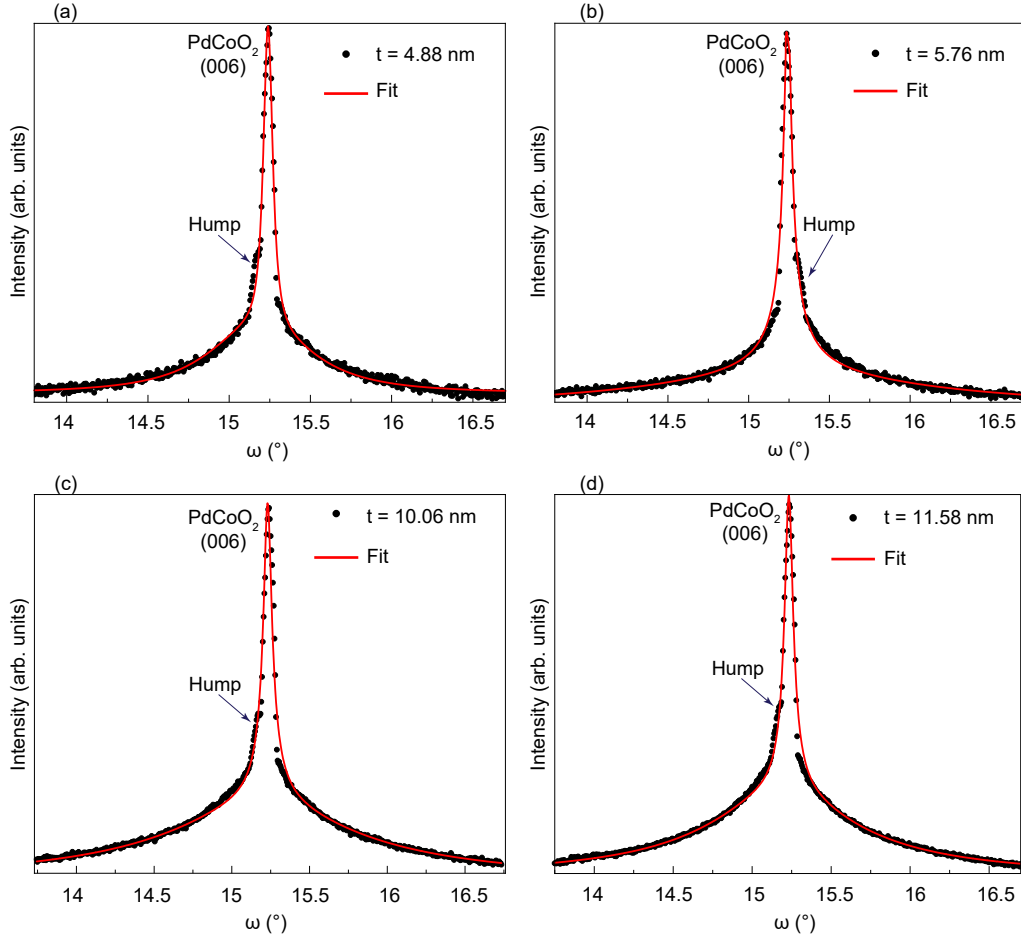


Figure S2: Fitted rocking curves around the (006) reflections of various PdCoO_2 films with different thicknesses (t). The full width at half maximum (FWHM) values plotted in Fig 1(f) of the main text were extracted from these fits. Note the consistent presence of a small hump in about 0.5° interval around the film peak.

IV. TEMPERATURE AND ANGLE DEPENDENT MAGNETOTRANSPORT

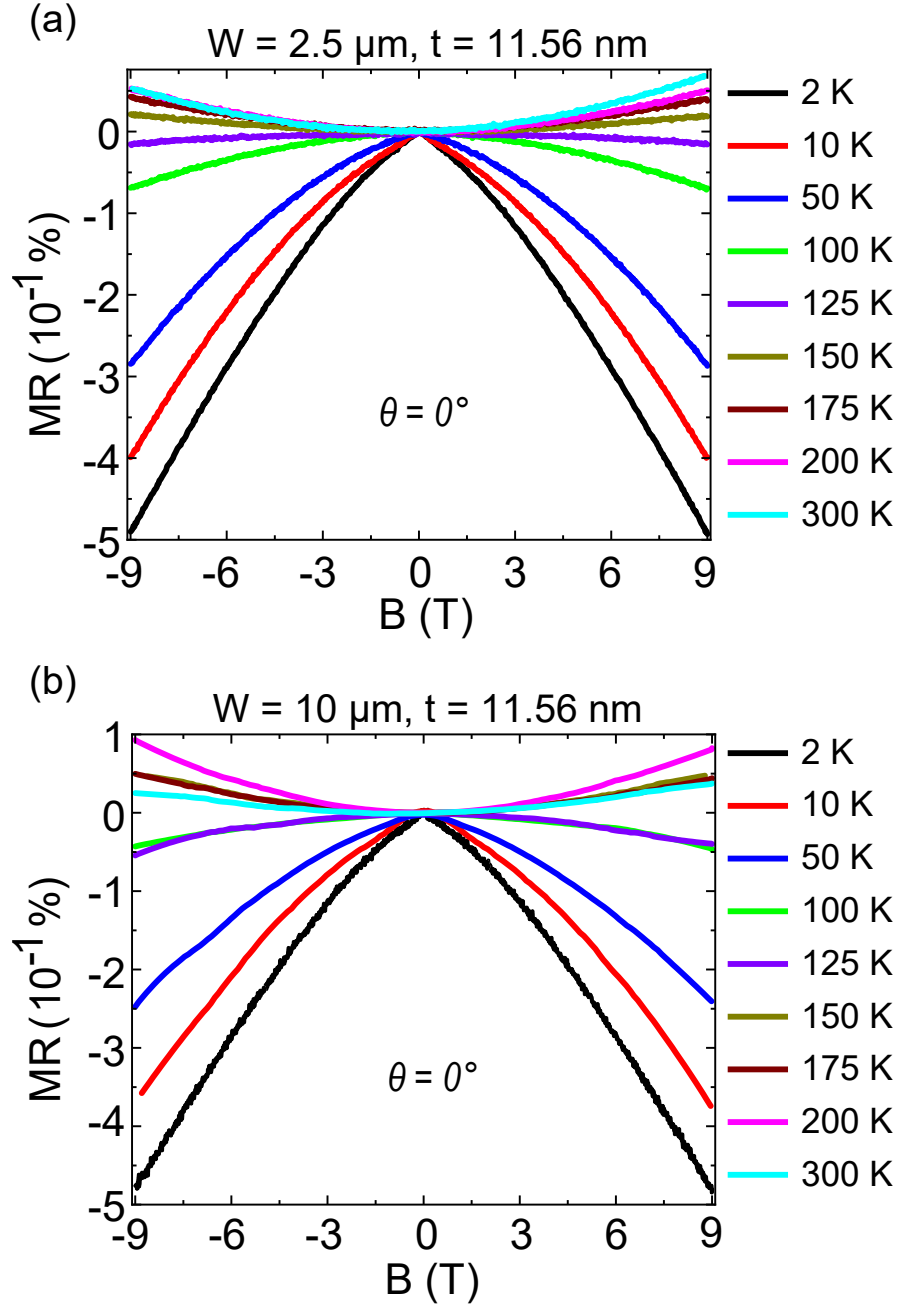


Figure S3: Temperature-dependent magnetoresistance data for the 11.56 nm thick sample, measured simultaneously from the (a) $2.5 \mu\text{m}$ and (b) $10 \mu\text{m}$ Hall bar devices with the magnetic field B parallel to the sample c -axis. Note here that the MR becomes positive at the temperature of 125 K, compared to 150 K in the thinner 4.88 and 5.26 nm samples.

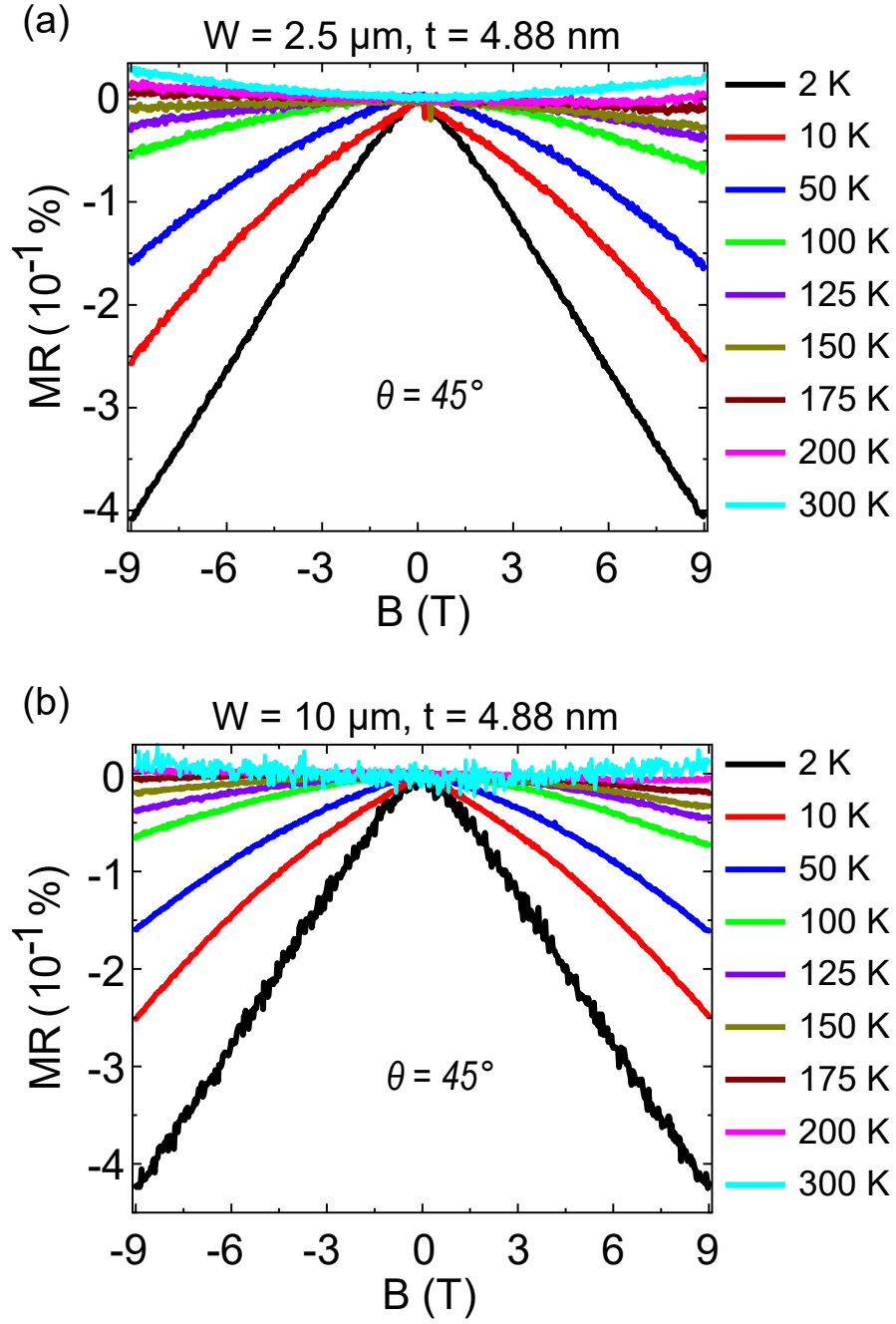


Figure S4: Temperature-dependent magnetoresistance data for the 4.88 nm sample, measured with the magnetic field B oriented 45° away from the sample c -axis. The data are acquired simultaneously from the (a) $2.5 \mu\text{m}$ and (b) $10 \mu\text{m}$ Hall bar devices. The MR data for this sample are the same whether B is 45° away from c or \parallel to c (see main text).

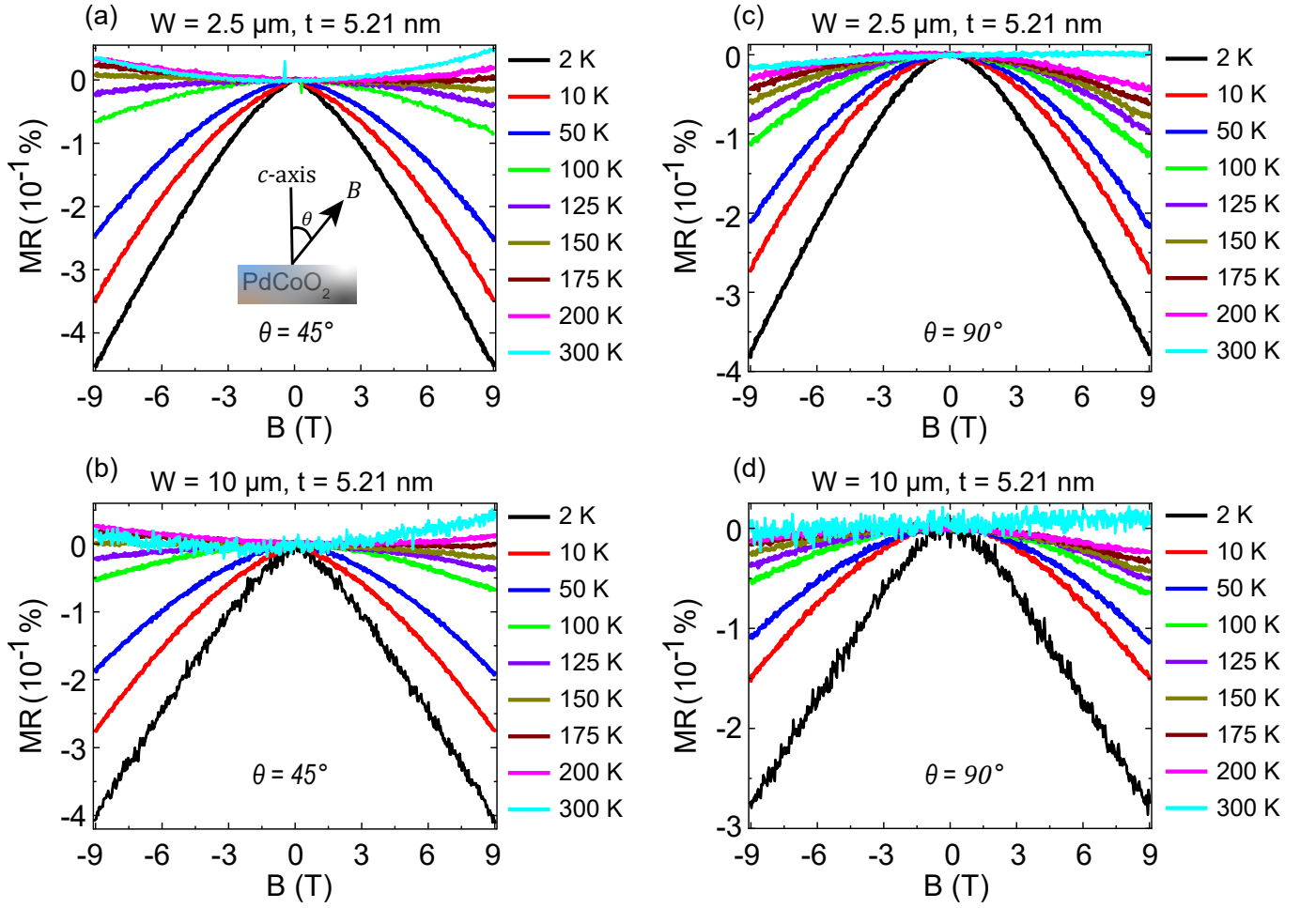


Figure S5: Temperature-dependent magnetoresistance data for the 5.21 nm sample measured with the magnetic field B oriented (a) and (b) 45° , and (c) and (d) 90° away from the sample c -axis. The data were measured from the $2.5 \mu\text{m}$ and $10 \mu\text{m}$ Hall bar devices, simultaneously in (a) and (b), and (c) and (d), respectively. Note the similarity between the data for both 4.88 nm and 5.21 nm samples, on both Hall bar devices and at the respective orientation of B .

V. ELECTRONIC TRANSPORT

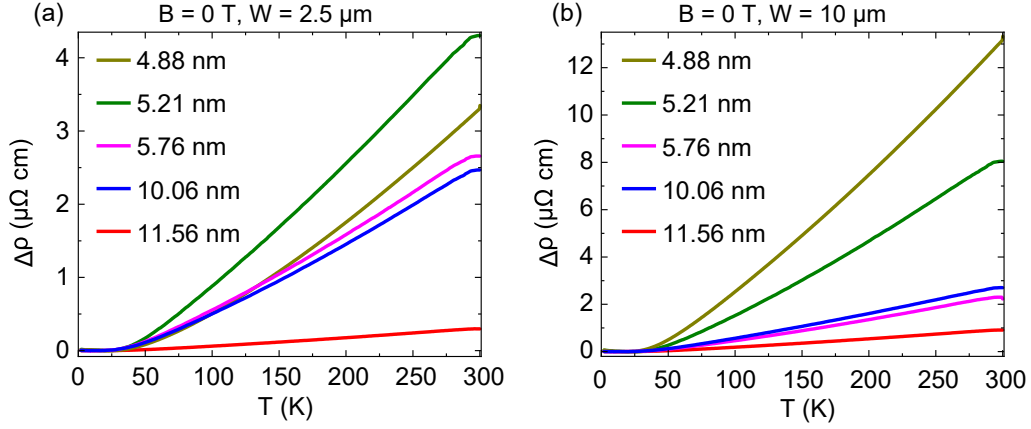


Figure S6: Relative temperature-dependence $\Delta\rho(T) = \rho(T) - \rho_0$ (with $\rho_0 = \rho(2\text{ K})$) of the resistivity for two Hall bar devices structured onto PdCoO₂ thin films of various thicknesses. This shows how the temperature-dependent part of the resistivity increases in magnitude as the thickness of the film decreases.

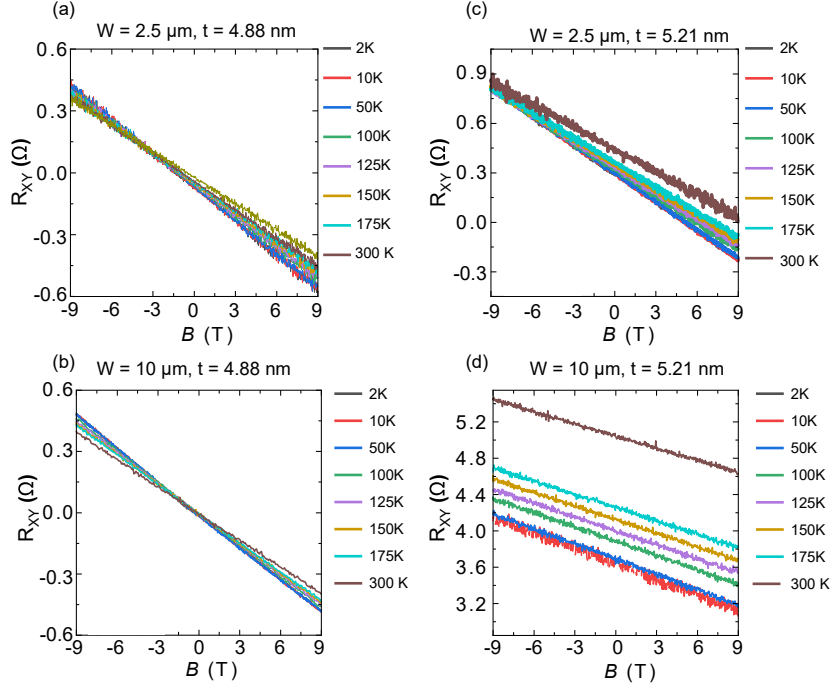


Figure S7: Temperature-dependent Hall resistivity $\rho_{xy}(B)$ measurements for two Hall bar devices structured onto PdCoO₂ thin films of thicknesses (a) and (b) 4.88 nm, and (c) and (d) 5.21 nm. The data were simultaneously acquired from the channel $W = 2.5$ and $10\text{ }\mu\text{m}$ in (a) and (b), and (c) and (d), respectively. All the Hall measurements were acquired with the magnetic field B applied parallel to the crystallographic c axis, i.e., perpendicular to the PdCoO₂ conducting planes. Note the linear slope of $\rho_{xy}(B)$ at all temperatures when B is swept from -9 to 9 T , indicating no sign of magnetism at the surface of the films [2].

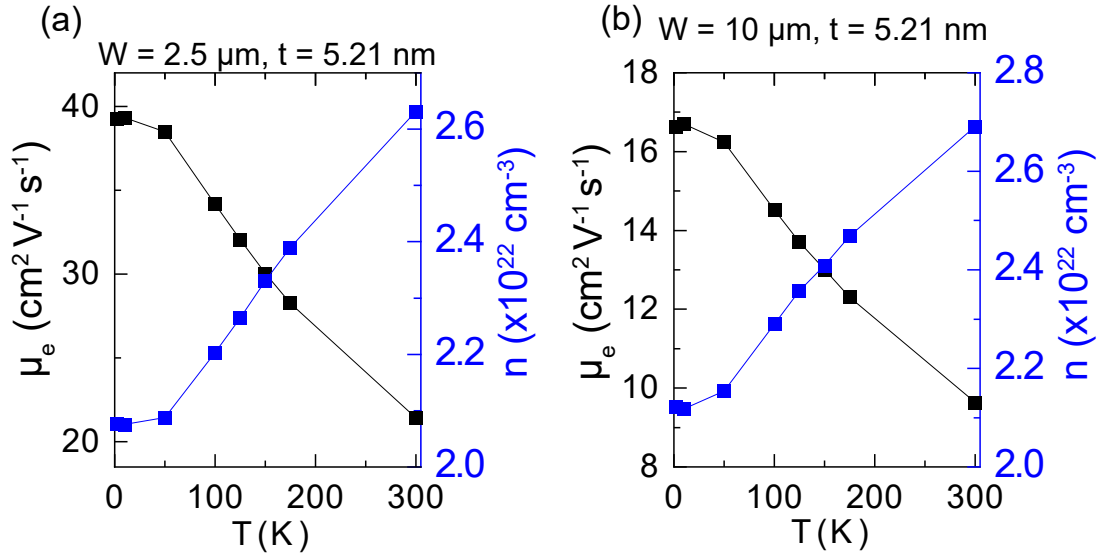


Figure S8: Temperature-dependent carrier densities and electron mobilities for the 5.21 nm thick PdCoO_2 sample. These data were simultaneously extracted from the Hall data shown in Fig. S4(c) and (d) above.

VI. REFERENCES

- [1]. Cueva, P., Hovden, R., Mundy, J. A., Xin, H. L. & Muller, D. A. *Data processing for atomic resolution electron energy loss spectroscopy. Microscopy and microanalysis : the official journal of Microscopy Society of America, Microbeam Analysis Society, Microscopical Society of Canada* **18**, 667 - 675; 10.1017/S1431927612000244 (2012).
- [2]. J. H. Lee, T. Harada, F. Trier, L. Marciano, F. Godel, S. Valencia, A. Tsukazaki, and M. Bibes, *Nano Lett.* **21**, 8687 (2021).